Available online at www.sciencedirect.com
SCIENCE DIRECT
Earth and Planetary Science Letters 238 (2005) 272–283
EPSL
www.elsevier.com/locate/epsl

A short timescale for changing oxygen fugacity in the solar nebula revealed by high-resolution ^{26}Al–^{26}Mg dating of CAI rims

Justin I. Simon [a,*], Edward D. Young [a,b], Sara S. Russell [c], Eric K. Tonui [a], Kathryn A. Dyl [a], Craig E. Manning [a]

[a] *Department of Earth and Space Sciences, UCLA, Los Angeles, CA 90095-1567, USA*
[b] *Institute of Geophysics and Planetary Physics, University of California Los Angeles, 595 Charles E. Young Drive East, 2676 Geology Building, Los Angeles, CA 90095, USA*
[c] *Department of Mineralogy, Natural History Museum, Cromwell Road London, SW7 7BD, UK*

Received 4 April 2005; received in revised form 1 August 2005; accepted 8 August 2005
Available online 19 September 2005
Editor: K. Farley

Abstract

Most rocky objects in the solar system, including the primitive chondrites and the terrestrial planets themselves, formed at oxygen fugacities (f_{O2}) near that of the Iron–Wüstite (IW) f_{O2} buffer. Conversely, the most ancient rocky objects of the solar system, the calcium aluminum-rich inclusions (CAIs), formed at f_{O2} values 5 orders of magnitude lower than the IW buffer in an environment more closely resembling a solar gas. High-resolution Mg isotope data and estimates for f_{O2} for rims on CAIs show that this shift from ~solar to protoplanetary (chondritic) f_{O2} occurred in 100,000 to 300,000 yr for these objects. Magnesium isotopes show further that the rise in f_{O2} was accompanied by a rise in the partial pressure of Mg. These results establish that CAIs entered a region resembling where planet progenitors formed within 3×10^5 yr of their formation in the solar nebula.

Keywords: solar nebula; timescales; Wark-Lovering rims; oxygen fugacity; mass-dependent isotope fractionation; Mg isotopes

1. Introduction

Refractory calcium aluminum-rich inclusions (CAIs) represent the most primitive record of rock formation in the solar system. Astrophysical models for the evolution of solids in the young solar protoplanetary disk must account for this record. Young protoplanetary disks in general evolve by viscous accretion to the star coupled with outward transport of angular momentum; as a consequence of viscous behavior, some disk materials spiral inwards towards the growing star while others move outward. How CAIs fit into this basic evolutionary picture of disk evolution is poorly understood. In this study we use

* Corresponding author. Tel.: +1 510 643 5061; fax: +1 510 642 9520.
E-mail address: simon@eps.berkeley.edu (J.I. Simon).

0012-821X/$ - see front matter © 2005 Elsevier B.V. All rights reserved.
doi:10.1016/j.epsl.2005.08.004

so-called Wark–Lovering rims on CAIs as a record of time-dependent changes in conditions in the solar protoplanetary disk.

Wark–Lovering (WL) rims [1] makeup the outermost portion of many CAIs. They consist of concentric bands tens of micrometers (μm) thick. Each band is composed of a distinctive mineralogy and they are often monomineralic. The bands comprise a characteristic mineralogical sequence that is independent of differences among CAI interiors. The normal sequence moving from the interior towards the edge of the CAI is spinel ± perovskite ± hibonite, ± melilite, Al-rich clinopyroxene, and ± forsterite. These enigmatic features have been studied for decades. Some workers suggest that the rims formed by condensation. Others conclude that they were evaporative residues. Their significance has proven elusive even as their ubiquity betrays their importance as a consequence of a process fundamental to the early solar nebula [1]. Here we use the amount of radiogenic ^{26}Mg (^{26}Mg*) due to decay of the extinct radionuclide ^{26}Al (mean life = 1.05 million yr) to date WL rim formation relative to CAI interiors. At the same time we apply measured Ti^{3+}/Ti^{4+} and $^{25}Mg/^{24}Mg$ as "cosmobarometers" to constrain the f_{O2} (oxygen fugacity) and P_{Mg} (partial pressure of Mg) attending growth of the CAIs and their rims. The picture that emerges is one of rapidly changing gas-phase conditions in the early solar system as recorded by the CAIs. This timescale can be compared with those for protoplanetary disk evolution in general.

The growth model for WL rim formation described herein is similar to the metasomatic model [2] in so far as both rely on large gradients in chemical potentials to drive the formation of the WL rims. In addition, both models invoke reaction between the CAI and a surrounding Mg and Si-rich gas. However, a metasomatic mechanism implies that refractory elements are scavenged from the interior while we show that growth could have occurred from elements in the gas phase alone. We show further that the new Mg isotope data for WL rims are more easily understood if the rims represent the product of growth that is chemically and isotopically independent from the host CAIs. Growth in response to high chemical potential gradients can explain both the uncoupling between interior and rim formation and the WL rim and host CAI Mg isotope data.

2. Analytical methods

2.1. Magnesium isotopes

Measurements of $^{25}Mg/^{24}Mg$, $^{26}Mg/^{24}Mg$ and $^{27}Al/^{24}Mg$ in the CAI interiors and rims were obtained by ultraviolet (UV) laser ablation combined with multiple-collector inductively coupled plasma-source mass spectrometry (MC-ICPMS) using methods described previously [3]. The laser was operated at a 213 nm fluence of 20 to 30 J/cm^2 and a pulse repetition rate of 1 to 2 Hz. Analytical spot size was varied between 50 and 100 μm depending upon Mg concentration. Rims were analyzed using 50 μm wide trenches measuring ~200 μm in length. Excess radiogenic^{26}Mg values were calculated from measured $^{26}Mg/^{24}Mg$ and $^{25}Mg/^{24}Mg$ expressed in the linear delta notation (δ') relative to the DSM3 magnesium standard [4] where $\delta^i Mg' = \ln((^iMg/^{24}Mg)_{sample}/(^iMg/^{24}Mg)_{DSM3})10^3$ and i represents either 25 or 26. On the DSM3 scale, $\delta^{25}Mg'$ of typical chondrite material (e.g., bulk CI meteorite) is 0.0 ‰. With these definitions for δ' values, radiogenic ^{26}Mg is quantified as $\delta^{26}Mg^* = \delta^{26}Mg' - \delta^{25}Mg'/(0.521)$ where 0.521 is the slope of the equilibrium mass-dependent isotope fractionation relationship between $\delta^{26}Mg'$ and $\delta^{25}Mg'(\beta)$. The exact value of the mass-dependent fractionation relationship depends upon physicochemical process and ranges from 0.521 to 0.511 [5]. Our conclusions are not altered by the choice of β value within this range because WL rims have $\delta^i Mg'$ values near zero. The use of multiple detectors and the sample-standard comparison method for correcting for instrumental mass bias affords routine analysis of samples that have $^{27}Al/^{24}Mg$ values less than five such as the WL rims [6]. Tests with solids and solutions show that within realistic elemental concentrations for CAIs matrix mass bias effects are well within the reproducibility (0.25‰/amu, 2 s.d.) of our solid–solid standard comparison method (cf. [6]). External reproducibility is estimated from repeated analyses of USNM 136718 forsterite, Burma spinel, and a synthetic fassaite glass (glass P10). A $^{48}Ca^{++}$ interference on $m/z = 24$ produces a consistent enrichment of ~0.04‰ in $\delta^{26}Mg^*$ per unit Ca/Mg. A correction for the interference was applied based on the Ca/Mg ratios of the analyzed materials as determined from their measured Al/Mg ratios and chemical for-

mulae (e.g., in melilite $Ca/Mg = 2/(1-x)$ where x is the mole fraction of the tschermak exchange component $Al_2Mg_{-1}Si_{-1}$ in the melilite). Tests with terrestrial melilites, vesuvianite, and glass P10 demonstrate that this correction scheme affords accurate results within the precision of the measurements.

2.2. Oxygen fugacity based on Ti^{3+}/Ti^{4+} in pyroxene

The f_{O2} values attending pyroxene growth in the interiors and the rims of the CAIs were determined from the ratio of the activity of $CaTi^{4+}Al_2O_6$ to the activity of $CaTi^{3+}AlSiO_6$ in pyroxene. This activity ratio defines f_{O2} by virtue of gas–solid equilibria involving O_2. The oxidation state of Ti was obtained by calculation of relative abundances of cations from electron microprobe analyses (UCLA Jeol superprobe) assuming no vacancies in the pyroxene formula. This approach has been shown to be robust for CAI pyroxenes because of the virtual absence of other multivalent cations (e.g., Fe) [7,8]. Twenty nine analyses of pyroxene in the WL rim of CAI 144A were obtained using a minimum electron beam size. The TiO_2 content (total Ti as TiO_2) of the rim pyroxenes varied between 2 and 7 wt.% with most analyses being above 4 wt.%. Twenty three analyses representing 3 different Ti-rich pyroxenes located in the interior of CAI 144A were obtained for comparison with the rims. Interior pyroxene contained 17–19 wt.% TiO_2. The amount of Ti^{3+} was calculated from total Ti based on oxygen excess in the cation-normalized formula (or cation deficiencies in the oxygen normalized formula). Reported uncertainties in the final cation assignments are based on a Monte Carlo error simulation ($n = 300$ trials) in which the uncertainties in the wt.% oxide data were propagated through the cation norm calculation. The algorithm for the integrated probability density function for a Gaussian distribution used to model uncertainties is described by Harbaugh and Bonham-Carter [9]. Random numbers generated to draw from parent populations for each oxide come from an algorithm described by Press et al. [10].

3. Calcium Aluminum-rich inclusions

Rims and interiors of three igneous CAIs from the Leoville and Allende CV3 carbonaceous chondritic meteorites were examined as part of this study. Allende 3576-1 "b" is a ~4 × 3.5 mm Type B CAI composed of intergrown melilite and pyroxene surrounded by a mantle dominated by melilite. Spinel is abundant throughout the inclusion. A WL rim that is ~30–60 μm thick and composed of spinel and pyroxene coats the melilite dominated interior. Leoville 144A is a compact, oval ~10 × 6 mm Type A CAI composed of fine grained intergrown melilite and rare Ti–Al-rich pyroxene that encloses abundant micron-sized perovskite grains. Spinel is distributed throughout the CAI. The WL rim of Leoville 144A is composed of an inner layer of Mg-rich spinel intergrown with platy crystals of hibonite, thin (<10 μm) discontinuous layers of melilite and calcic pyroxene and an outer layer composed predominantly of Al-rich pyroxene. The spinel in the inner layer encloses numerous small perovskite grains. The thickness of the outer pyroxene layer as presented in the polished surface used for these analyses varies from <50 to ~200 μm. Leoville MRS3 is a fragment of a Type A CAI measuring ~0.7 mm in length and 0.5 mm in width. It is largely composed of coarse grained melilite with subordinate spinel. The WL rim of MRS3 is <50–100 μm thick and is composed of an inner layer of spinel and an outer layer of Al-rich pyroxene.

4. Magnesium isotope ratios in Wark–Lovering rims and interiors of CAIs

4.1. ^{26}Al as a chronometer

The one-time presence of ^{26}Al in the solar system is evidenced by excesses of its decay product, $^{26}Mg^*$ (^{26}Al decays to radiogenic ^{26}Mg, $^{26}Mg^*$, primarily by β^+ emission and also by electron capture), correlated with Al/Mg in the constituents of meteorites [11]. The use of ^{26}Al as a chronometer relies on variations in the initial $^{26}Al/^{27}Al$, hereafter $(^{26}Al/^{27}Al)_0$, in objects formed within several mean lives of ^{26}Al decay. Values for $(^{26}Al/^{27}Al)_0$ are defined by isochrons comprising linear correlations between $^{26}Mg^*/^{24}Mg$ (expressed as $\delta^{26}Mg^*$, the per mil deviation in $^{26}Mg/^{24}Mg$ from the value corresponding to mass-dependent isotope fractionation) and $^{27}Al/^{24}Mg$. The slopes of these isochrons are numerically equivalent to $(^{26}Al/^{27}Al)_0$ since all of the ^{26}Al decayed away

billions of years ago. Age differences are reflected in differences in $(^{26}Al/^{27}Al)_0$ if the initial $^{26}Al/^{27}Al$ was uniform in the early solar system. Recent UV laser ablation and acid digestion MC-ICPMS analyses of CAIs [3,6,12,13] show that the $(^{26}Al/^{27}Al)_0$ for CAIs in the early solar system was at least 6×10^{-5} and possibly as high as 7×10^{-5} (but see Bizzarro et al. [14]), and that the canonical $(^{26}Al/^{27}Al)_0$ of 4.5×10^{-5} is a value representing the time at which heating of CAIs ceased.

Our UV-MC-ICPMS data show that the WL rims formed within ~300,000 yr of the first CAI interiors (Table 1). Measurements of WL rims from Leoville 144A, Leoville MRS3 and Allende 3576-1 "b" define an Al–Mg isochron corresponding to an $(^{26}Al/^{27}Al)_0$ value of 5.3 $(\pm0.8)\times10^{-5}$ with a $\delta^{26}Mg^*$ intercept of zero (0.06 ± 0.1) (Fig. 1). Interiors of the Leoville CAIs display well-defined $(^{26}Al/^{27}Al)_0$ of at least 6×10^{-5} [3] (Appendix A, an electronic supplement). The data for the Allende inclusion are less well behaved (apparently due to alteration) but are consistent with the Leoville results. From the difference between the rim $(^{26}Al/^{27}Al)_0$ value and those representing growth of the CAI interiors the time interval between initial CAI growth and rim formation can be constrained from the expression $(5.3\times10^{-5})/(6.0\times10^{-5})=\exp(-\lambda\ \Delta t)$. The Δt obtained is 130,000 yr based on a decay constant λ of 9.52×10^{-7} yr^{-1}. This value may be a minimum. The $(^{26}Al/^{27}Al)_0$ of the interior of Leoville 144A could have been as high as 7×10^{-5} meaning that Δt could have been as large as 290,000 yr. Alternatively, if ^{26}Al is heterogeneous in the early solar system, then the time difference is likely to be even smaller.

4.2. $^{25}Mg/^{24}Mg$ as a cosmobarometer

CAI interiors and rims have markedly different $\delta^{25}Mg'$ suggestive of distinctly different P_{Mg} during their formation. Interiors of the three igneous CAIs have $\delta^{25}Mg'$ values significantly greater than the 0‰ (±1) that characterizes Earth, Moon, and most constituents of chondritic meteorites [5,15]. The WL rims, on the other hand, have $\delta^{25}Mg'\leq0$‰ irrespective of the $\delta^{25}Mg'$ values of the enriched interiors (Fig. 2).

The depleted $\delta^{25}Mg'$ compositions observed in the WL rims indicate that they are condensates formed at relatively high P_{Mg} while the high $\delta^{25}Mg'$ values of

Table 1
Laser ablation Mg isotope data for Wark–Lovering rims on CAIs from CV carbonaceous chondrites

Analysis	Phase(s)	Location from rim (μm)	$^{27}Al/^{24}Mg$	σ_m	$\delta^{25}Mg'$	σ_m	$\delta^{26}Mg'$	σ_m	$\delta^{26}Mg^*$	σ_m
Allende (3576-1″b″)										
Spot 20	W–L>>mel	−50	0.57	0.03	−0.86	0.19	−1.53	0.12	0.12	0.32
Spot 21	W–L>>mel	−50	0.24	0.02	−1.30	0.15	−1.81	0.14	0.69	0.19
Leoville (144A)										
Line 3	W–L Al–Ti diopside	−100	0.76	0.04	−0.09	0.12	0.11	0.06	0.27	0.23
Line 4	W–L Al–Ti diopside	−75	1.04	0.09	−1.74	0.11	−2.74	0.11	0.60	0.17
Line 5	W–L Al–Ti diopside	−150	0.94	0.01	−0.38	0.17	−0.48	0.13	0.25	0.28
Line 6	W–L hb sp	−50	0.91	0.04	−0.85	0.11	−1.33	0.12	0.30	0.19
Line 7	W–L Al–Ti diopside	−120	0.96	0.02	−1.29	0.09	−2.32	0.19	0.16	0.15
Line 8	W–L hb sp	−25	1.31	0.07	−1.97	0.14	−3.39	0.10	0.39	0.29
Leoville (MRS3)										
Line 1	W–L Al–Ti diopside	−20	4.62	0.54	−0.45	0.12	0.81	0.26	1.67	0.32
Line 2	W–L Al–Ti diopside	0	9.02	0.70	−0.98	0.31	2.09	0.38	3.97	0.49

Measurements are a mixture of WL rim phases; dominant phase is indicated when known. Excess radiogenic ^{26}Mg values were calculated from measured $^{26}Mg/^{24}Mg$ and $^{25}Mg/^{24}Mg$ expressed in the linear delta notation (δ') relative to the DSM3 magnesium standard where $\delta^i\ Mg'=\ln((^iMg/^{24}Mg)_{sample}/(^iMg/^{24}Mg)_{DSM3})10^3$ and i represents either 25 or 26 (CI chondrite=0.0‰ on the DSM3 scale [5]). With these definitions for δ' values radiogenic ^{26}Mg is $\delta^{26}Mg^*=\delta^{26}Mg'-\delta^{25}\ Mg'/(0.521)$ where 0.521 is the slope of the equilibrium mass-dependent isotope fractionation relationship between $\delta^{26}Mg'$ and $\delta^{25}Mg'$. Interior Mg isotope measurements can be found in the electronic supplement.

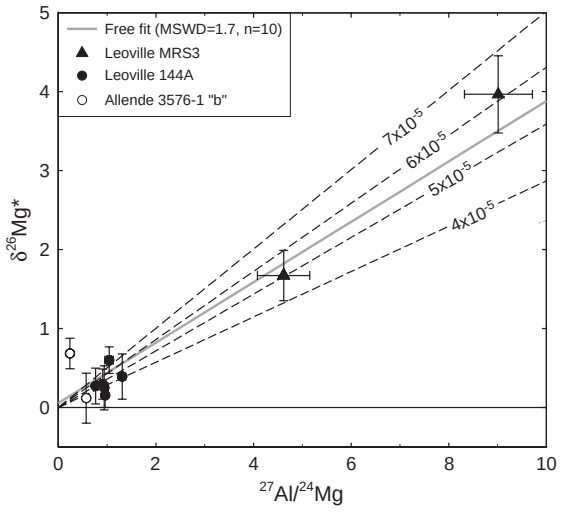

Fig. 1. The Al–Mg evolution of WL rims as defined by those measured from Leoville 144A, Leoville MRS3, and Allende 3576-1 "b" (best fit for initial $^{26}Al/^{27}Al = 5.3 \times 10^{-5} \pm 0.8$, $1\sigma_m$, MSWD = 1.7, $n = 10$). Dashed lines for reference $^{26}Al/^{27}$ Al values as indicated. The Mg data for WL rims were obtained in situ by UV laser ablation MC-ICPMS, reported in Table 1. Measurements were obtained as ~50 μm diameter spots and ~50 μm wide line scans. Reported uncertainties are $1\sigma_m$.

the interiors of these igneous CAIs (the igneous CAIs were once molten in space) shows that they are evaporative residues formed at lower P_{Mg} [16] (Fig. 2). The role of Mg isotope ratios as Mg barometers is seen with reference to an equation that governs the net flux of Mg volatilized from a molten sphere [17], rewritten in the form [5]:

$$J_{Mg,net} = \frac{J_{Mg,evap}\left(1 - \frac{P_{Mg,\infty}}{P_{Mg,sat}}\right)}{1 + \Gamma} \quad (1)$$

in which,

$$\Gamma = \frac{\gamma_{Mg} r}{D_{Mg,gas}} \sqrt{\frac{RT}{2\pi m_{Mg}}} \quad (2)$$

and where $J_{Mg,net}$ is the net difference between the evaporative and condensation fluxes for Mg (Mg evaporates as Mg gas), $J_{Mg,evap}$ is the evaporative flux of Mg, $P_{Mg,\infty}$ is the partial pressure of Mg far removed from the molten object, $P_{Mg,sat}$ is the saturation partial pressure of Mg, $D_{Mg,gas}$ is the diffusion coefficient of Mg through the gas phase, γ_{Mg} is the evaporation factor for Mg, r is the radius of the molten object, and m_{Mg} is the mass of the volatilizing species. In terms of this equation, isotope fractionation will occur when $J_{Mg,net}/J_{Mg,evap} \rightarrow 1$ while no fractionation occurs when $J_{Mg,net}/J_{Mg,\ evap} \rightarrow 0$. The latter occurs where the background pressure $P_{Mg,\infty}$ approaches the saturation pressure $P_{Mg,\ sat}$. This could be the case where a population of volatilizing liquid spheres contributes to an elevated background of partial pressure of rock-forming elements by virtue of a relatively high number density. In the other extreme where $P_{Mg,\ sat} >> P_{Mg,\ \infty}$, as would be the case where objects

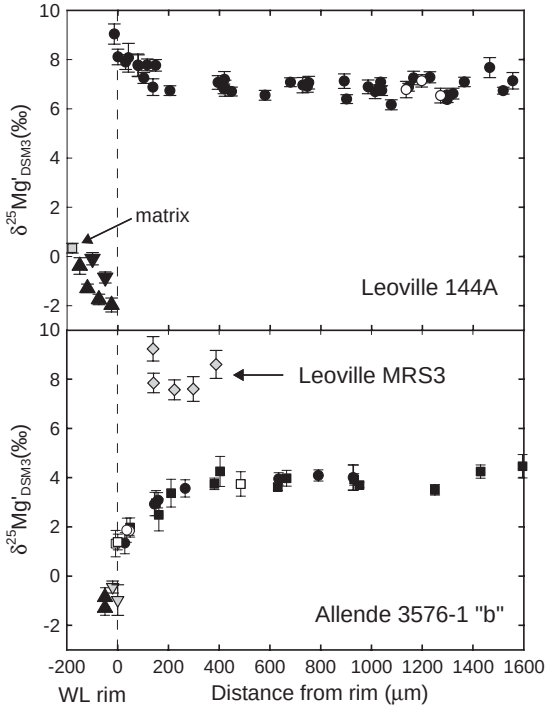

Fig. 2. Systematic variations in intrinsic Mg isotope ($\delta^{25}Mg'$) composition obtained by in situ laser ablation core-to-rim traverses of studied CAIs. All CAIs possess WL rims that have low $\delta^{25}Mg'$ compositions relative to chondritic, but exhibit interiors with $\delta^{25}Mg'$ higher than chondritic values by ~3‰ to > 6‰. Closed symbols are melilite, open symbols are pyroxene, and triangles are WL rims, unless labeled otherwise. (Top) Six radial traverses of Leoville 144A exhibit a progressively enriched edge (< 200 μm), a flat bottom interior, and a reproducible subchondritic WL rim that exhibits outward per mil enrichment converging on chondrite. (Bottom) Seven analyses of Leoville MRS3 are consistent with those of Leoville 144A and three radial traverses of Allende 3675-1 "b" yield a progressively depleted margin (~500 μm), a flat topped interior and a subchondritic WL rim. Reported uncertainties are $2\sigma_m$.

are not sufficiently close together to cause a pervasive rise in background partial pressures, the only way to prevent fractionation is for Γ, and therefore total gas pressure, to be large (e.g., [12]). The kinetic theory of gases permits one to express Γ as a function of pressure. Such calculations show that Γ is large enough to preclude fractionation when total pressures approach 1 bar (e.g., using experimental values for γ_i=0.06 [18], Γ=~10^{-2} at 10^{-3} bar and ~10 at 1 bar for a millimeter-sized object). From these considerations it is clear that the level of isotopic fractionation for a major rock-forming element like Mg in an object that was once molten in the early solar system is seen to be a barometer of either total pressure (large Γ) or partial pressures relative to saturation (small Γ).

Eqs. (1) and (2) show that high δ^{25}Mg′ in the interior of the once molten CAIs is a consequence of evaporation where P_{Mg} and total pressure were both low, and that the lack of Mg isotope fractionation among virtually all other rocky objects, including the WL rims and the millimeter-sized chondrules that were molten and free-floating in the nebula, signifies P_{Mg} values approaching saturation or high total pressures. Since the pressures required to raise Γ to sufficiently high values to preclude fractionation are several orders of magnitude greater than estimates for the nebula (~10^{-3} bar maximum, e.g., [19]), P_{Mg} approaching saturation ($P_{\mathrm{Mg,sat}}$) is indicated.

4.3. Wark–Lovering rims are nebular condensates

Wark–Lovering rims have chondritic and subchondritic δ^{25}Mg′ values signifying that they, like the chondules and unlike CAIs interiors, formed at partial pressures of Mg approaching saturation. This in turns suggests that they formed by condensation. Wark and Lovering originally attributed the rims to nebular condensation, but after finding enrichments of rare earth elements (REE) and other refractory trace elements in rims, Wark and Boynton argued that rims were residues of intense (>2500 K) and brief (<2 s) thermal events that evaporated surface material from CAIs [20] that were then subsequently altered by a metasomatic process where inter-diffusion with later accreted olivine grains occurred (i.e., [2]). Wark and Boynton correctly recognized that spinel and Ti–Al-pyroxene in the rims exhibit the same range of ^{16}O-rich compositions as the interiors, and have therefore not exchanged with, or been diluted by, greater amounts of "normal" oxygen (e.g., [21,22]). A similar, but more compelling argument can be made from Mg based on the fact that rims have excess ^{26}Mg. They also have even lower δ^{25}Mg′ than the surrounding matrix. Evaporation followed by accretion does not explain the low δ^{25}Mg′ of the rims. The enrichments in REE that are sometimes observed in the rims can be explained by the greater abundance of minerals that retain REE (primarily perovskite) stabilized by the condensation reactions. The present study suggests that the factor that stabilized pervasive perovskite in the rims may have been oxidation of Ti from Ti^{3+} to Ti^{4+}. In short, our high-precision Mg isotope data show that the WL rims are condensates and not evaporative residues.

5. A general model for Wark–Lovering rim formation

Ruzicka [2] and MacPherson and others [23] recognized the importance of large gradients in chemical potentials (μ_i) as the principal driving force for WL rim formation. Both studies emphasized the role of metasomatism (i.e., Si and Mg diffusion into the CAI). Here we consider that the isotope and f_{O2} data for rims are consistent with new mineral growth and present thermodynamic calculations that reproduce the WL rim sequence as products of growth in high μ_i gradients.

Thermodynamic calculations show that the characteristic sequence in WL rim mineralogy (spinel ± hibonite → Al-rich diopside → forsterite) is explained by placing solid melilite-rich CAI interiors at elevated temperature (≥1400 K) into a region that imposes high positive gradients in μMg (P_{Mg}) (and μSiO (P_{SiO})) and μO_2 (f_{O2}). The effects of high μMg and f_{O2} can be seen in a phase diagram that shows the stability fields of minerals in the model system Ca–Mg–Al–Si–O as a function of the partial pressures of the gas species Mg, Ca, SiO, and O_2 (Fig. 3). For the purposes of illustration, Fig. 3 shows a section at fixed P_{SiO}. Similar diagrams can be constructed in which P_{SiO} is a variable. Partial pressures in Fig. 3 refer to a total standard state pressure of 1 bar, i.e., the P_i values are mole fractions at any total pressure. Solid lines delimit stability fields for anorthite, spinel,

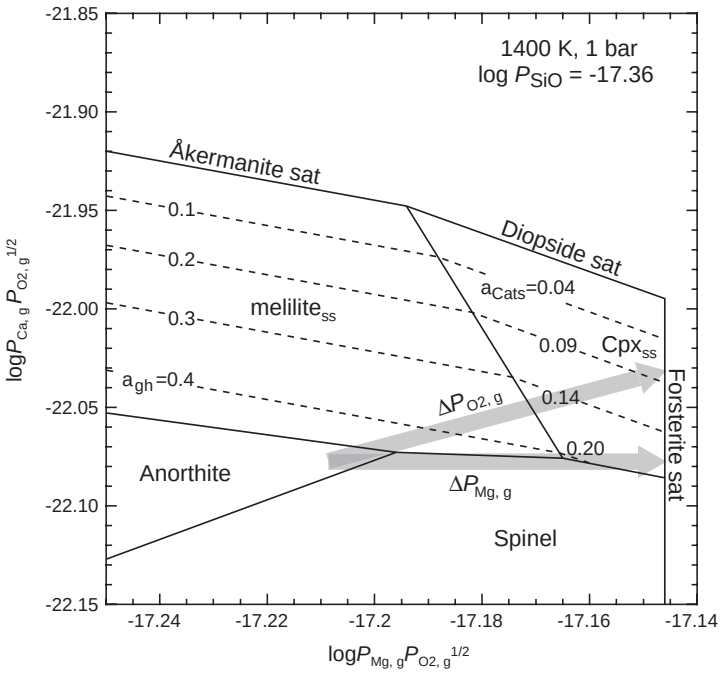

Fig. 3. Phase diagram of mineral stability in the model system Ca–Mg–Al–Si–O. This activity–activity diagram illustrates mineral growth expected during interaction of a CAI with an infinite reservoir of forsterite (i.e., chondritic)–equilibrated gas. Arrows indicates the sequence of mineral banding that will develop by evaporation–precipitation reactions where log$P_{Mg,\,g}$ and log$P_{O2,\,g}$ increase, respectively. Phase relations derived at 1400 K, 1 bar total pressure, using tabulated thermodynamic data [10,32], standard states of unit activity of pure minerals at all P and T and ideal gases at 1 bar and T, and an ideal-mixing-on-sites approximation for activities of solid solution components.

melilite and clinopyroxene. Lines defining the Al-free end members åkermanite, diopside, and forsterite represent saturation surfaces (solid lines). Gases with partial pressure (mole fractions) products higher than these limiting lines are metastable (supersaturated) with respect to these solid phases. Dashed lines represent isopleths of gehlenite and Ca-tschermak activities in melilite and clinopyroxene, respectively.

The model in Fig. 3 shows that a rise in P_{Mg} and P_{O2} (f_{O2}) at fixed P_{Ca} (fixed partial pressure of Ca is expected since Ca is refractory and evaporation of rock dust would result in relatively negligible transfer of Ca to the gas phase) will produce the general sequence of mineral zones found in WL rims. Changes in temperatures and/or partial pressures of SiO, Mg, Ca, and/or O_2 along the reaction path would produce variations in the rim mineralogy. For example, polythermal growth of the rims is a satisfactory explanation for the presence or absence of a significant melilite layer between spinel and Al-rich pyroxene because the melilite stability field will expand or contract substantially with changes in temperature. Moreover, initially higher temperatures can explain the origin of hibonite in the inner layer.

In any case, the phase diagram predicts that a rise in the partial pressures of the major chondritic rock-forming elements Mg and O will lead to mineralogies resembling WL rims. The low δ^{25}Mg′ of the WL rims relative to their host CAIs is an indication that P_{Mg} was indeed relatively high during rim formation. We should expect that if WL rims grew by large increases in P_{Mg} that there should be evidence for a comparable rise in f_{O2}. The evidence for this increase in f_{O2} is discussed next.

6. Oxidation state of Wark–Lovering rims

Titanium is usually present in terrestrial and extraterrestrial samples as Ti^{4+}. In CAIs there is appreciable Ti^{3+} as well as Ti^{4+} in pyroxenes. The presence of

Table 2
Representative pyroxene compositions for CAI 144A

Analysis	WL rim		WL rim		Interior	
Measured	wt.%	σ_m	wt.%	σ_m	wt.%	σ_m
SiO_2	42.26	0.13	34.62	0.12	31.60	0.11
Al_2O_3	16.71	0.08	23.54	0.09	19.69	0.09
TiO_2	2.50	0.05	7.66	0.08	17.85	0.13
Ti_2O_3	0.00	0.00	0.00	0.00	0.00	0.00
FeO	1.32	0.04	1.08	0.04	0.00	0.00
Cr_2O_3	0.09	0.04	0.19	0.04	0.08	0.04
MnO	0.00	0.00	0.00	0.00	0.00	0.03
MgO	11.77	0.06	10.14	0.06	7.04	0.05
CaO	24.17	0.10	23.54	0.10	24.52	0.10
Na_2O	0.11	0.02	0.05	0.02	0.00	0.00
K_2O	0.04	0.02	0.04	0.02	0.01	0.01
Total	98.96		100.86		100.80	
Cations formula based on 6 oxygen atoms						
Si	1.559		1.267		1.172	
Al	0.727		1.016		0.861	
Ti^{4+} = Total	0.069		0.211		0.498	
Fe	0.041		0.033		0.000	
Cr	0.003		0.005		0.002	
Mn	0.000		0.000		0.000	
Mg	0.647		0.553		0.389	
Ca	0.955		0.923		0.974	
Na	0.008		0.004		0.000	
K	0.002		0.002		0.000	
Total	4.011		4.014		3.896	
Recalculated...	wt.%	σ_m	wt.%	σ_m	wt.%	σ_m
SiO_2	42.26	0.13	34.62	0.12	31.61	0.11
Al_2O_3	16.71	0.08	23.55	0.09	19.70	0.08
TiO_2	3.72	0.27	9.21	0.26	6.88	0.22
Ti_2O_3	−1.10	0.25	−1.39	0.24	9.87	0.22
FeO	1.33	0.04	1.08	0.04	0.00	0.00
Cr_2O_3	0.09	0.04	0.19	0.04	0.08	0.04
MnO	0.00	0.00	0.00	0.00	0.00	0.03
MgO	11.77	0.06	10.14	0.05	7.04	0.05
CaO	24.17	0.11	23.55	0.10	24.52	0.10
Na_2O	0.11	0.02	0.05	0.02	0.00	0.00
K_2O	0.04	0.02	0.04	0.02	0.01	0.01
Total	99.09		101.03		99.71	
Tetrahedral cations						
Si	1.555	0.004	1.263	0.004	1.203	0.004
Al	0.445	0.003	0.737	0.003	0.797	0.003
Total	2.000		2.000		2.000	
Octahedral cations						
Al	0.280	0.003	0.275	0.003	0.087	0.003
Ti^{4+}	0.103	0.008	0.253	0.007	0.197	0.006
Ti^{3+}	−0.034	0.008	−0.042	0.007	0.314	0.007
Fe	0.041	0.001	0.033	0.001	0.000	0.000
Cr	0.003	0.001	0.005	0.001	0.002	0.001
Mn	0.000	0.000	0.000	0.000	0.000	0.001
Mg	0.645	0.003	0.551	0.003	0.399	0.002
Ca	0.953	0.003	0.920	0.003	1.000	0.003
Na	0.008	0.001	0.004	0.001	0.000	0.000
K	0.002	0.001	0.002	0.001	0.000	0.000
Total	2.001		2.001		1.999	
Ti^{3+}/Ti^{4+}	−0.33	0.05	−0.17	0.03	1.60	0.08
$\log f_{O2}$	−14.53	0.64	−13.01	0.60	−19.26	0.10

Measurements are representative WL rim and interior pyroxene compositions. The amount of Ti^{3+} is calculated from Ti^{4+} based on oxygen excess in the cation-normalized formula. Reported uncertainties are $1\sigma_m$ based on Monte Carlo error simulation (n = 300 trials, see text for details).

Ti^{3+} signifies reducing conditions similar to solar values of f_{O2} [8]. In this study f_{O2} values for the rim and interior of CAI 144A were determined using electron microprobe analyses of Ti-bearing pyroxene grains (representative analyses can be seen in Table 2). The ratio of the activity of $CaTi^{4+}Al_2O_6$ to the activity of $CaTi^{3+}AlSiO_6$ in pyroxene defines f_{O2} by virtue of gas–solid equilibria involving O_2. For pyroxene in the interior of the CAI where melilite is abundant we rely upon two pyroxene–melilite–gas equilibria calibrated previously by Beckett and Grossman [8]. The first is the reaction

$$4\underset{di}{CaMgSi_2O_6} + 4\underset{T4Cats}{CaTi^{4+}Al_2O_6} = 4\underset{T3Cats}{CaTi^{3+}AlSiO_6} + 2\underset{ak}{Ca_2MgSi_2O_7} + 2\underset{Sp}{MgAl_2O_4} + \underset{gas}{O_2} \quad (3)$$

and the second is

$$2\underset{Cats}{CaAl_2SiO_6} + 2\underset{di}{CaMgSi_2O_6} + 4\underset{T4Cats}{CaTi^{4+}Al_2O_6} = 4\underset{T3Cats}{CaTi^{3+}AlSiO_6} + 2\underset{gh}{Ca_2Al_2SiO_7} + 2\underset{Sp}{MgAl_2O_4} + \underset{gas}{O_2}\,. \quad (4)$$

In both reactions di, Cats, T4Cats and T3Cats refer to the indicated components in pyroxene and ak and gh to the components in melilite. In the WL rims melilite is scarce to absent and we employ a different reaction involving pyroxene and gas alone:

$$2\underset{\text{di}}{CaMgSi_2O_6} + 4\underset{\text{T4Cats}}{CaTi^{4+}Al_2O_6} + 2\underset{\text{gas}}{SiO} = 2\underset{\text{Cats}}{CaAl_2SiO_6} + 4\underset{\text{T3Cats}}{CaTi^{3+}AlSiO_6} + 2\underset{\text{gas}}{Mg} + \underset{\text{gas}}{O_2}\,. \quad (5)$$

A systematic study of the accuracy of the thermodynamic data for the Ti-bearing components in pyroxene has not been undertaken. The uncertainties in these thermochemical data are removed in the case of reaction (5) if the equilibrium constant is expanded in differential form. The equilibrium for reaction (5) leads to the expression

$$\log f_{O2} = 4\log\left(\frac{a_{T4Cats}}{a_{T3Cats}}\right) + 2\log\left(\frac{a_{di}}{a_{Cats}}\right) + 2\log\left(\frac{P_{SiO}}{P_{Mg}}\right) - \frac{\Delta G^0_{rxn}}{2.3RT} \quad (6)$$

where ΔG^0_{rxn} is the Gibbs free energy for the reaction at a standard state of pure solids and ideal gases at 1 bar, R is the ideal gas constant, T is temperature, and a_i is the activity of the indicated component i. The influence of the uncertainties in $\Delta G_{rxn}{}^0$ is removed by taking the derivative of the $\log f_{O2}$ in (6), recognizing that the coefficients on the right-hand side are the partial derivatives of $\log f_{O2}$ with respect to the logarithms of the indicated activity ratios. The resulting expression is

$$\log f_{O2} = \log f^0_{O2} + 4\Delta\log\left(\frac{a_{T4Cats}}{a_{T3Cats}}\right) + 2\Delta\log\left(\frac{a_{di}}{a_{Cats}}\right) + 2\Delta\log\left(\frac{P_{SiO}}{P_{Mg}}\right) \quad (7)$$

where $\log f^0_{O2}$ refers to some initial condition, in this case the $\log f_{O2}$ of the CAI interiors. This last equation permits contouring of $\log f_{O2}$-temperature space for $\log(a_{Ti4+}/a_{Ti3+})$ in Ti-rich pyroxene in the absence of melilite (see Fig. 4). The problem is simplified further by recognizing that changes in P_{Mg} will be attended by concomitant changes in P_{SiO} (since the source of both is most likely silicate dust), meaning that the last term is insignificant where changes in orders of magnitude of f_{O2} are of interest.

All three equilibria shown above were evaluated using activities based on ideal mixing on the octahedral site (in accord with the coupled mixing on the octahedral and tetrahedral sites in the pyroxenes and melilites associated with the tschermak exchange mechanism). In the cases of reactions (3) and (4) we used a fixed mole fraction of ak in melilite of 0.2 as indicated by electron microprobe analyses of melilites in the margin of Leoville CAI 144A. The results are robust relative to changes in ak content. Electron microprobe analyses were obtained from 22 Ti-rich pyroxene spots in the interior and from 29 relatively Ti-rich pyroxene spots in the WL rim of Leoville 144A. A complete data set is included in Appendix A, an electronic supplement.

Interior Ti-rich pyroxenes have an average Ti^{3+} cations per 6 oxygens of 0.31 ± 0.01 2σ (Fig. 4), indicating f_{O2} values just below those defined by a solar gas [24]. In contrast, the Ti-rich pyroxenes of the WL rims yield a much lower average Ti^{3+} content of -0.03 ± 0.02 2σ cations per 6 oxygens with most points exhibiting no detectable Ti^{3+} (Slightly negative values for Ti^{3+} result from cation sums per 6 oxygens greater than 4. All such instances are within the uncertainties of the measurements). The IW f_{O2} buffer curve coincides with the loss of detectable Ti^{3+} in pyroxene. As a result, absence of detectable Ti^{3+} in the WL rims places a lower limit on the f_{O2} of their formation at or ~1 log units below the IW buffer. The lack of Ti^{3+} in the WL rims suggests that they formed at a minimum of ~6 to 7 log units higher f_{O2} than the CAI interiors (Fig. 4); the WL rims formed at f_{O2} indistinguishable from most chondrites, Earth, Mars, and Moon [25,26].

These results can be related back to the phase equilibrium model for WL formation in Fig. 3. The figure shows that WL rim formation could have been driven by a shift to higher P_{O2} (f_{O2}) relative to the

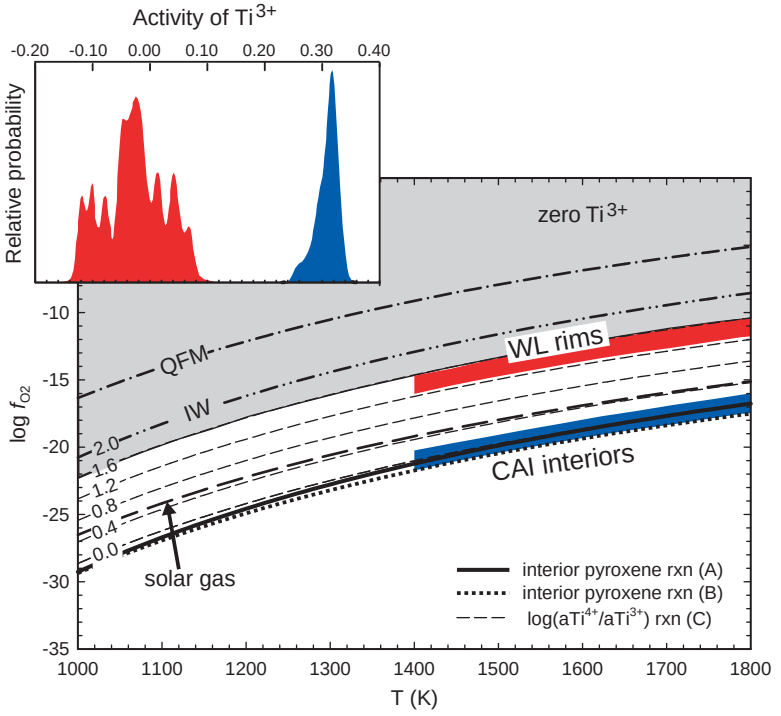

Fig. 4. Log f_{O2} versus temperature for average CAI interior and WL rim measurements based on Ti^{3+} in pyroxene. The inset shows the distribution of Ti^{3+} activity for interiors (near zero) and rims (~0.30). For substitution in the octahedral site of pyroxene the activity of Ti^{3+} is the mole fraction and therefore numerically equivalent to the number of Ti^{3+} atoms per 6 oxygen atoms (i.e., ideal mixing-on-sites activity model). Also shown are the Quartz–Magnetite–Fayalite (QFM) buffer, Iron–Wüstite (IW) buffer, and a curve representing a gas of solar composition. Calculated contours (light dashed lines) for the log of the activity ratio of T4Cats to T3Cats in 0.4 log unit intervals are shown for reference (see text for details).

CAI interiors. This requisite rise in f_{O2} is recorded by the pyroxenes in the rim of CAI 144A.

7. Rapid changing conditions in the solar nebula

Collectively, our observations imply a common nebular origin for WL rims by a process different from those that created the CAI interiors. Our findings provide evidence for two distinct episodes of nebular CAI evolution: (1) evaporation at low total pressure, low solar-like f_{O2}, and low P_{Mg} and (2) condensation to form the WL rims at high f_{O2} (~IW) and high P_{Mg}. The commonly accepted explanation for enhancing P_{O2} and P_{Mg} is evaporation of chondritic dust in the nebula [27]. The question arises as to whether these differences reflect changing conditions at a particular place in the nebula, as for example where CAIs remain in the hot inner nebula for long periods of time (e.g., [28]) or transport from one environment to another (e.g., [29,30]). This work affords constraints on the applicability of these different models by comparing high-resolution age constraints with large shifts in ambient conditions during the formation of Wark–Lovering rims on CAIs.

The simple explanation for these data is that WL rims are condensates formed when CAIs passed from low pressures of a solar-like gas into regions of chondritic dust enrichment. Both the lack of Mg isotope fractionation and the high f_{O2} are explained in this scenario. High P_{O2} and P_{Mg} are taken as evidence for dust enrichment relative to a solar gas. The initial $^{26}Al/^{27}Al$ of 5.3×10^{-5} for the rims places temporal constraints on this movement from one reservoir to another if the $(^{26}Al/^{27}Al)_0$ for the solar system was uniform; the transition took 100,000 to 300,000 yr. Alternatively, these data constrain the degree of ^{26}Al heterogeneity in the solar nebula. CAIs and their rims

formed in markedly different conditions yet they have similar $(^{26}Al/^{27}Al)_0$ values of 6×10^{-5} to 7×10^{-5} and 5.3×10^{-5}, respectively. If the CAIs formed in the inner annulus of the protoplanetary disk near the *x*-point for example [31], where gas resembled a solar composition, and then were transported outwards to make WL rims in the part of the protoplanetary disk where chondrites and ultimately planets accreted, then the measured $(^{26}Al/^{27}Al)_0$ ratios limit the degree of heterogeneity in this parameter; the disparate regions of the nebula had a limited range in $(^{26}Al/^{27}Al)_0$ of $\sim7\times10^{-5}$ to $\sim5\times10^{-5}$. In any case, the CAIs moved from a reducing solar-like gas to a more oxidizing region of chondritic dust enrichment in 3×10^5 yr, or less.

Acknowledgments

We gratefully acknowledge A. Ruzicka and an anonymous referee for their helpful and constructive reviews. Financial support for this project provided by NSF and NASA's Cosmochemistry program and the NASA Astrobiology Institute.

Appendix A. Supplementary data

Supplementary data associated with this article can be found, in the online version, at doi:10.1016/j.epsl.2005.08.004.

References

[1] D. Wark, J.F. Lovering, Marker events in the early evolution of the solar system: evidence from rims on Ca–Al-rich inclusion in carbonaceous chondrites, Proc. Lunar Planet. Sci. Conf., 8th (1977) 95–112.

[2] A. Ruzicka, Mineral layers around coarse-grained, Ca–Al-rich inclusions in CV3 carbonaceous chondrites: formation by high-temperature metasomatism, J. Geophys. Res. 102 (1997) 13,387–13,402.

[3] E.D. Young, J.I. Simon, E. Tonui, S.S. Russell, O. Lovera, Supra-canonical $^{26}Al/^{27}Al$ and the residence time of CAIs in the solar nebula, Science Express Research Articles, 2005, pp. 1108140.

[4] A. Galy, O. Yoffe, P.E. Janney, R.W. Williams, C. Cloquet, O. Alard, L. Halicz, M. Wadhwa, I.D. Hutcheon, E. Ramon, J. Carignan, Magnesium isotope heterogeneity of isotopic standard SRM980 and new reference materials for magnesium-isotope ratio measurements, J. Anal. At. Spectrom. 18 (2003) 1352–1356.

[5] E.D. Young, A. Galy, The isotope geochemistry and cosmochemistry of magnesium, in: J.J. Rosso (Ed.), Geochemistry of Non-Traditional Stable Isotopes, vol. 55, Mineralogical Society of America, 2004, pp. 197–230.

[6] E.D. Young, R.D. Ash, A. Galy, N.S. Belshaw, Mg isotope heterogeneity in the Allende meteorite measured by UV laser ablation–MC-ICPMS and comparisons with O isotopes, Geochim. Cosmochim. Acta 66 (2002) 683–689.

[7] E. Stolper, J. Paque, G.R. Rossman, The influence of oxygen fugacity and cooling rate on the crystallization of Ca–Al-rich inclusions from Allende, LPSC XXI (1982) (abstr. 77).

[8] J.R. Beckett, L. Grossman, Oxygen fugacities in the solar nebula during crystallization of fassaite in Allende inclusions, LPSC XXV (1986) (abstr. 36).

[9] J.W. Harbaugh, G. Bonham-Carter, Computer Simulation in Geology, vol. 69, Wiley-Interscience, 1970, pp. 82–84.

[10] W.H. Press, B.P. Flannery, S.A. Teukolsky, W.T. Vetterling, Numerical Recipes The Art of Scientific Computing, Cambridge University Press, 1986, 818 pp.

[11] T. Lee, D.A. Papanastassiou, G.J. Wasserburg, Demonstration of ^{26}Mg excess in Allende and evidence for ^{26}Al, Geophys. Res. Lett. 3 (1976) 109–112.

[12] A. Galy, E.D. Young, R.D. Ash, R.K. O'Nions, The formation of chondrules at high gas pressures in the solar nebula, Science 290 (2000) 1751–1753.

[13] A. Galy, I.D. Hutcheon, L. Grossman, $(^{26}Al/^{27}Al)_0$ of the solar nebula inferred from Al-Mg systematics in bulk CAIs from CV3 chondrites, LPSC XXXV (2004) (abstr. 1790).

[14] M. Bizzarro, J.A. Baker, H. Haack, Mg isotope evidence for contemporaneous formation of chondrules and refractory inclusions, Nature 431 (2004) 275–278.

[15] P.H. Warren, E.K. Tonui, E.D. Young, Magnesium Isotopes of Lunar Rocks and Glasses and Implications for Origin of the Moon, LPSC XXXVI (2005) (abstr. 2143).

[16] A.M. Davis, A. Hashimoto, R.N. Clayton, T.K. Mayeda, Isotope mass fractionation during evaporation of Mg_2SiO_4, Nature 347 (1990) 655–658.

[17] F.M. Richter, A.M. Davis, Elemental and isotopic fractionation by diffusion-limited evaporation, LPSC XXXV (2004) (abstr. 2047).

[18] F.M. Richter, A.M. Davis, D.S. Ebel, A. Hashimoto, Elemental and isotopic fractionation of type b calcium-, aluminum-rich inclusions: experiments, theoretical considerations, and constraints on their thermal evolution, Geochim. Cosmochim. Acta 66 (2002) 521–540.

[19] S. Yondea, L. Grossman, Condensation of $CaO–MgO–Al_2O_3–SiO_2$ liquids from cosmic gases, Geochim. Cosmochim. Acta 59 (1995) 3413–3444.

[20] D. Wark, W.V. Boynton, The formation of rims on calcium–aluminum-rich inclusions: step I—flash heating, Meteorit. Planet. Sci. 36 (2001) 1135–1166.

[21] K.D. McKeegan, L.A. Leshin, G.J. MacPherson, Oxygen-isotopic stratigraphy in a vigarano type A calcium–aluminum-rich inclusion, Meteorit. Planet. Sci. 33 (1998) 102–103.

[22] E.D. Young, S.S. Russell, R.D. Ash, Ultraviolet laser ablation measurements of oxygen isotope ratios in a Leoville compact type A CAI, LPSC XXXI (2000) (abstr. 1837).
[23] G.J. MacPherson, L. Grossman, J.R. Beckett, J.M. Allen, Origin of rims on coarse-grained inclusions in the Allende meteorite, LPSC XX (1981) (abstr. 12).
[24] A.N. Krot, B.J. Fegley, K. Lodders, H. Palme, Meteoritical and astrophysical constraints on the oxidation state of the solar nebula, in: V. Mannings, A.P. Boss, S.S. Russell (Eds.), Protostars and Planets IV, The University of Arizona Press, Tucson, 2000, pp. 1019–1054.
[25] M.N. Spilde, J.J. Papike, Pyroxenes from lunar high-Ti mare basalts: oxygen analysis by electron microprobe and estimates of Ti^{3+}/Ti^{4+}, LPSC XXVII (1996) (abstr. 1249).
[26] J.J. Jones, Redox conditions among the terrestrial planets, LPSC XXXV (2004) (abstr. 1264).
[27] D.S. Ebel, L. Grossman, Condensation in dust-enriched systems, Geochim. Cosmochim. Acta 64 (2000) 339–366.
[28] J.N. Cuzzi, S.S. Davis, A.R. Dobrovolskis, Blowing in the wind: II. Creation and redistribution of refractory inclusions in a turbulent protoplanetary nebula, Icarus 166 (2003) 385–402.
[29] F.H. Shu, H. Shang, M. Gounelle, A.E. Glassgold, T. Lee, The origin of chondrules and refractory inclusions in chondritic meteorites, Astrophys. J. 548 (2001) 1029–1050.
[30] A.P. Boss, Mixing and transport of chondrules and CAIs in the solar nebula, LPSC XXXVI (2005) (abstr. 1024).
[31] F.H. Shu, H. Shang, T. Lee, Towards an astrophysical theory of chondrites, Science 271 (1996) 1545–1552.
[32] T.J.B. Holland, R. Powell, An internally consistent thermodynamic data set for phases of petrological interest, J. Metamorph. Geol. 16 (1998).